Formation of large grains by epitaxial and abnormal growth at the surface of pulsed electron beam treated metallic samples

Ping Yan, Thierry Grosdidier, Xiangdong Zhang, Jianxin Zou

Materials and Design 159 (2018) 1–10

Contents lists available at ScienceDirect

Materials and Design

journal homepage: www.elsevier.com/locate/matdes

Formation of large grains by epitaxial and abnormal growth at the surface of pulsed electron beam treated metallic samples

Ping Yan [a], Thierry Grosdidier [b,c,*], Xiangdong Zhang [d,1], Jianxin Zou [a,**]

[a] National Engineering Research Center of Light Alloy Net Forming (NERC-LAF), State Key Lab of Metal Matrix Composites, Shanghai Jiao Tong University, 800 Dongchuan Road, Shanghai 200240, PR China
[b] Université de Lorraine, Laboratoire d'Etude des Microstructures et de Mécanique des Matériaux (LEM3 UMR 7239), 7 rue Félix Savart, Metz F-57073, France
[c] Université de Lorraine, Laboratory of Excellence on Design of Alloy Metals for low-mass Structures (Labex DAMAS), 7 rue Félix Savart, Metz F-57073, France
[d] Key Laboratory of Materials Modifications by Laser, Ion and Electron Beams, Dalian University of Technology, Dalian, PR China

HIGHLIGHTS

- Extremely large (mm) grains were obtained at the surface of pulsed electron beam treated metallic samples.
- These millimetric grains formed in Al alloys by the combination of epitaxial growth and abnormal grain growth.
- Epitaxial growth leads to solidified grains having sizes and crystallographic orientations inherited from the substrate.
- The driving force for abnormal grain growth is the difference in defects generated at each irradiation on cooling.

GRAPHICAL ABSTRACT

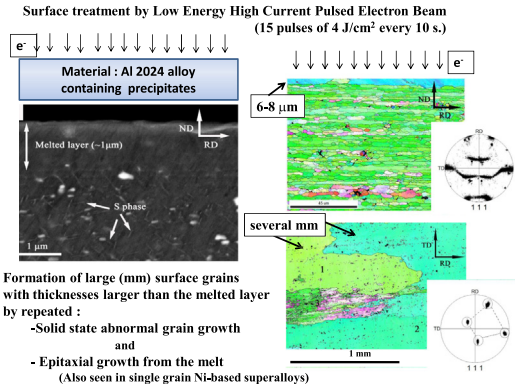

ARTICLE INFO

Article history:
Received 4 May 2018
Received in revised form 1 August 2018
Accepted 18 August 2018
Available online 19 August 2018

Keywords:
Surface treatment
High current pulsed electron beam (HCPEB)
Epitaxial growth
Abnormal grain growth
Al 2024 alloy
Single grain superalloys

ABSTRACT

The aim of the present work was to clarify that the rapid solidification process involved during surface pulsed beam treatment does not necessarily leads to the formation of nano or ultrafine grains. To demonstrate this, two types of metallic materials (a slightly deformed 2024 aluminum alloy and nickel based single grain superalloys) have been irradiated 15 times by high current pulsed electron beam. Epitaxial growth was triggered during the re-solidification of the superalloys, leading to the formation of a deformed single grain. Thanks to the repeated combinations of epitaxial growth and solid state secondary recrystallization, the pulsed electron beam treatment has led to the formation of large (millimetric) grains, that were also 4 to 5 times thicker than the depth of the melted zone, at the surface of the aluminum alloy.

1. Introduction

Initially developed in Tomsk (Russia) at the Institute of High Current Electronics [1–3], the high-current electron beam (HCEB) technology has now attracted much attention for material surface modifications.

* Correspondence to: T. Grosdidier, Université de Lorraine, Laboratoire d'Etude des Microstructures et de Mécanique des Matériaux (LEM3 UMR 7239), 7 rue Félix Savart, Metz F-57073, France.
** Corresponding author.
E-mail addresses: pingyan@sjtu.edu.cn (P. Yan), thierry.grosdidier@univ-lorraine.fr (T. Grosdidier), zoujx@sjtu.edu.cn (J. Zou).
[1] Now with the China Academy of Engineering Physics, Mianyang, PR China.

https://doi.org/10.1016/j.matdes.2018.08.033
0264-1275/

The pulsed electron beam technology employed in the present manuscript uses low energy (up to about 40 keV), high-current (up to about 50 kA) electron beams of microsecond durations that can treat a rather large surface area of about 100 mm in diameter. For surface modifications, this type of extremely short pulse treatment is often repeated over 5 to 50 cycles and generally induces the formation of three successive zones in the irradiated samples. If the energy imparted to the sample is sufficiently high, the very top surface (few microns) consists generally of a melted and rapidly solidified layer from which some light element may have evaporated [4]. Below is present a heat affected zone (~10 μm) where solid-state phase transformations and recrystallization may occur [5,6]. Finally, much deeper within the surface (~100 μm), can be present a zone that is affected by the generated stresses and which can be hardened by plastic deformation and the presence of structural defects such as vacancies and dislocations [7–10] as well as by the formation of stress induced martensite [11,12] or deformation twins [13,14].

After its development in Russia, this technology - and very close ones - has spread towards Asia (China, Japan, Korea), Europe and America. Because of its pulsed nature and the relative low energy of the electron beam that spreads in one shot over a large area, this technology has received a number of different types of acronyms depending of the types of rigs and applications: low energy high-current electron beam (LEHCEB) [1–3,15], (low energy) high current pulsed electron beam ((LE)HCPEB) [5,8–12,16], pulsed electron beam (pulsed EB) [17] as well as large-area electron beam (LAEB) [18–20] or large pulsed electron beam (LPEB) [21,22].

When the top surface is melted, because of the heat extraction towards the sub-surface, the solidification process can lead to solidification rates as high as 10^7 K/s [15,23]. Under such rapid solidification conditions, metastable phase transformations can occur which may harden the top surface [24,25], Also, when sufficient number of pulses are used in multiphase alloys (in particular those reinforced by precipitates), the repeated melting can homogenize the chemistry of the top surface, which generally leads to improved corrosion properties [26–30]. It has also been claimed in several contributions that the rapid solidification process inevitably leads to significant grain refinement down to the "nanometer" or, more rigorously, the sub-micrometer range. Indeed, ultrafine and nanoscale precipitates and domains [31–33], ultrafine and nano-grains [34–36] and nanostructures [37–39] are regularly reported on a wide variety of metals. Comparatively, Samih et al. [40] reported the formation of large grains, up to 50 μm in diameter, at the surface of a AISI 420 martensitic stainless steel. This clearly means that the formation of ultrafine grains is not necessarily associated with such type of treatment. To demonstrate this, from our understanding of the HCPEB surface modifications, we present here an analysis of the surface modification at the surface of an aluminum alloy for which the formation of large grains, having a size reaching the mm range, has been triggered. At the light of some analyses carried out on HCPEB treated single crystal superalloys, the formation of these very large grains will be discussed in terms of epitaxial growth of the melted liquid from the substrate followed by solid state abnormal grain growth.

2. Experimental procedure

2.1. Materials selection

2.1.1. The 2024 alloy sheets

A commercial 2024 Al alloy was used in this investigation. This alloy is an Al-Cu-Mg based alloy used essentially for aircraft application in the form of plates or sheets. The exact chemical composition of the 2024 alloy used in the present investigation is as follows (wt%): Al-4.3%Cu-1.5%Mg-0.6%Mn-0.3%Fe-0.3%Si. This 2024 alloy was delivered to us in the form of 10 mm thick rolled sheet. Then, the sheet was treated under the so called T9 condition - homogenized, aged then cold worked - before the HCPEB surface treatment. The alloy was homogenized at 500 °C for 1 h followed by water-quenching. Subsequently, the sheet was aged at 200 °C for 3 h and cold rolled to a reduction ratio of 15% by four successive passes carried out along the same rolling direction (RD).

2.1.2. The Ni-based single grain superalloys

The Ni-base superalloys used here are the so-called CMSX2 [41] and AM1 [42] alloys. The nominal chemical compositions of the AM1 and CMSX2 alloys are (wt%): Ni-7.5%Cr-5.5%W-8%Ta-5.3%Al-6.5%Co-1.2% Ti-2%Mo and Ni-8%Cr-8%W-6%Ta-5.6%Al-4.6%Co-1%Ti-0.6%M [43]. These alloys have been developed by the aircraft industry for directional solidification as single grain turbine blades. Thus, due to the absence of grain boundary, they could contain a high fraction of ordered γ′ precipitates dispersed in a face centered cubic (fcc) Ni based γ matrix without any other carbide or additional grain boundary strengthening phase. The superalloys were grown as single grain using the Brigman method in the shape of cylindrical rods having a diameter of 10 mm. The growth direction (GD) was along their [001] crystallographic direction. After solidification, they received a conventional optimization treatment in order to optimize the volume fraction and distribution of the coherent γ′ precipitates within the γ-Ni-based matrix [42]. Because of their high volume fraction (65 to 70%) and their coherency with the γ matrix, these γ′ precipitates adopt a cuboidal shape (with a mean edge size of about 0.4 μm) and are aligned in rows along the three ⟨001⟩ directions [42]. They were investigated here for two major reasons. Firstly, because of their ability to be cast as single grains that will be used to witness epitaxial grain growth during the HCPEB treatment. Secondly, because they are strengthened by coherent precipitates that were expected to witness the high temperature thermal cycles on heating (dissolution) [43]. It was also demonstrated recently that these coherent precipitates contained in superalloys do not induce the formation of a high density of craters under HCPEB [40]; craters that would potentially modify the local stress and, thereby, the solidification or solid state modifications on cooling [13].

2.2. HCPEB treatment

The HCPEB treatments were carried out using a "HOPE-1" source [16,30], a modified version of the Nadezhda-2 type source initially developed in Tomsk [3]. The following treatment parameters were used: energy densities of 4 J/cm^2 (for the Al alloy) or 6 J/cm^2 (for the superalloys) and a pulse duration of 1.5 μs. A number of 15 pulses (each separated by about 10 s) was used for the treatments. Small 10 × 10 × 8 mm specimens of the 2024 alloy were sampled from the sheet and the HCPEB treatment was applied with the electron beam parallel to the Normal direction of the sheet (perpendicular to the TD-RD plane). For the superalloys, the samples for HCPEB treatment were 2 mm-thick slices cut perpendicularly to the rod axis. Thus, the HCPEB treatment was carried out perpendicular to the rod axis with the electron beam directed along the [001] GD of the single grain. Before all the HCPEB treatments, the surfaces of the different samples were ground by using SiC sandpapers, followed by a polishing with diamond paste and finally with an OPS solution to ensure a high quality initial surface state (R_a about 0.05 μm).

2.3. Microstructure characterization

Surface and cross-sectional microstructures of the samples were observed by using a JEOL-7800F type SEM. The information about the microstructure and texture state of HCPEB-treated surface were also obtained by the JEOL-6500F type field emission gun scanning electron microscope (FEG-SEM), equipped with an electron back-scattering diffraction (EBSD) attachment (produced by Oxford). EBSD observations of the HCPEB treated sample surfaces were carried out without any further additional surface treatment. For cross sectional observations,

samples were grinding from cross section using sandpapers, polished with diamond paste and a silicon dioxide suspension.

3. Results

3.1. Effect of HCPEB on the 2024 Al alloy

Figs. 1 and 2 depict the main important features of the microstructure of the 2024 alloy substrate (before HCPEB); features that will be important to understand the microstructure formation mechanisms after the HCPEB treatment.

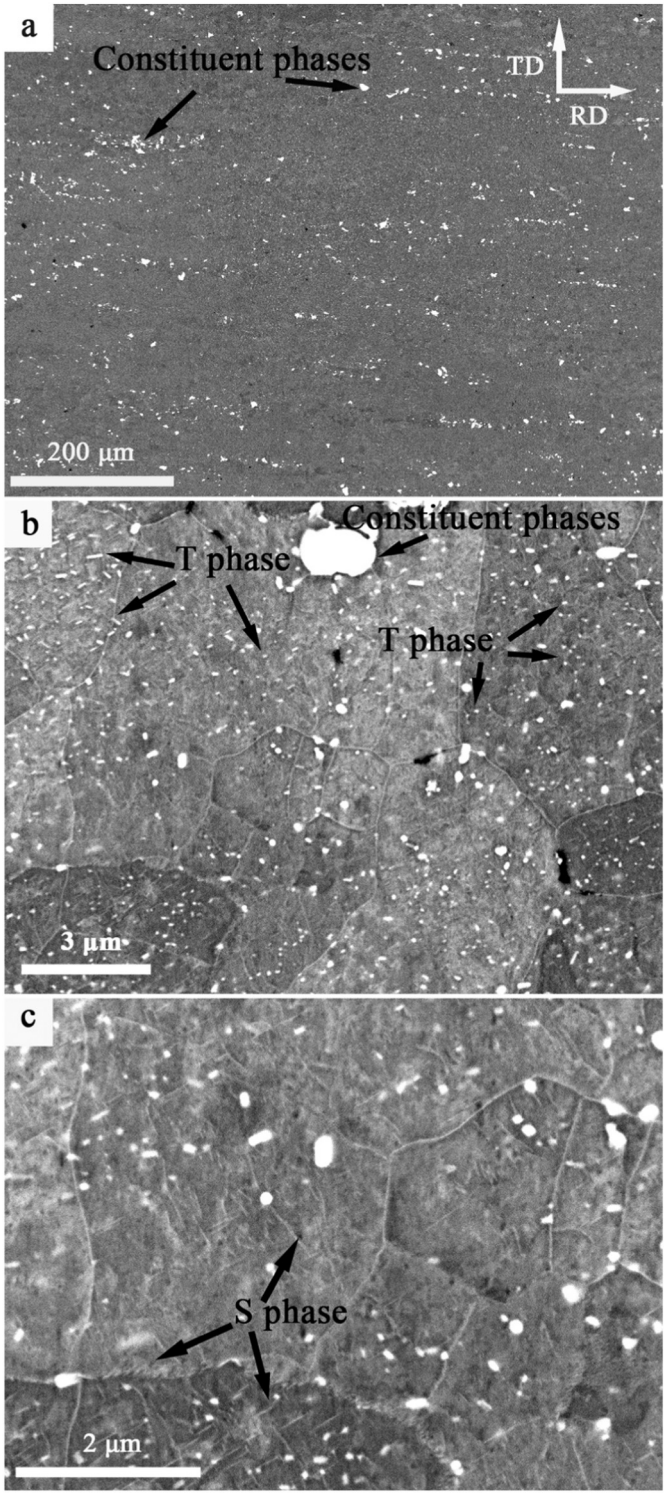

Fig. 1. BSE images of the 2024-T9 sample in different magnification: 150× (a), 8000× (b) and 17,000× (c).

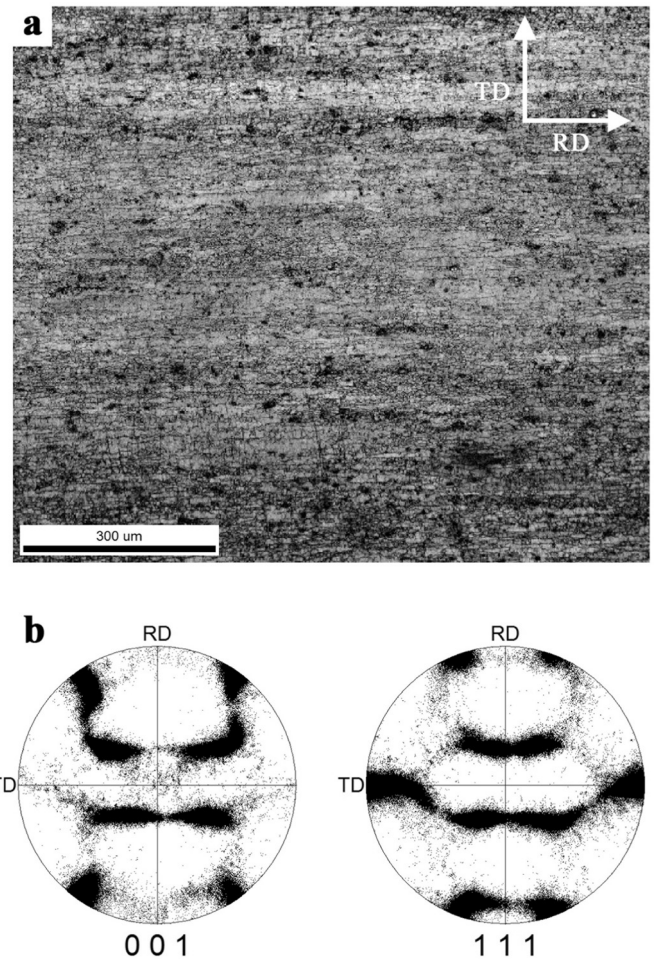

Fig. 2. EBSD maps and pole figures of the 2024-T9 sample: Kikuchi band contrast map (a) and pole figures (b).

Fig. 1 gathers SEM images taken at different magnifications illustrating the aspect of the microstructure in terms of grain size and shape as well as precipitate natures. From the low magnification micrograph in Fig. 1a, it is clear that the grains are rather slightly elongated in the rolling direction and, from Fig. 1b and c, that they contain subgrains having a size in the range 2–8 μm. Large particles, 0.5 to 8 μm in size, having rather irregular shapes and aligned along the extrusion direction are visible with white contrast in Fig. 1a. These particles, also referred to as the constituent particles [44], formed during the eutectic reaction at the end of the solidification process of the ingot and became aligned along the deformation direction during the warm rolling. The exact nature of these types of particles for the 2024-T3 alloy have been investigated in detail by Buchheit et al. [45] who showed that they are of 4 types of intermetallic compounds with a majority (about 60%) of the S-phase (Al_2CuMg) and $Al_6(Cu, Fe, Mn)$ particles (about 12%) followed by the Al_7Fe_2Cu and $(Al, Cu)_6Mn$ compounds. It is well established that some of these particles are insoluble during the homogenization heat treatment because of the low solubility of Fe and/or Si [45,46]. An example of these large particle is also visible in the upper part of Fig. 1b. Fig 1b and c, taken at higher magnifications, also reveal that the large grains contain sub-grains as well as two other types of secondary phases. Much smaller than the constituent particles and having a characteristic rodlike shape, are the T-phase dispersoids. These dispersoids are formed by a solid state transformation during the long term homogenization heat treatment [47]. In the 2 × 24 alloys, the main dispersoids are from the $Al_{20}Cu_2Mn_3$ phase [44] and, because of the

presence of Mn, this phase does not dissolve to an appreciable extent by subsequent solid state thermal treatment. Thus, one of its main role is to control the grain and sub-grain sizes by preventing recrystallization. Some of these dispersoids are arrowed in Fig. 1b and c. Finally, the highest magnification in Fig. 1c reveals the presence of fine precipitates that formed during ageing at 200 °C. They have a lath type of structure typical of the S-phase (Al_2CuMg). They formed from the supersaturated solid solution (SSS) via the formation of Guinier-Preston-Bagaryatsky (GPB) zones and S″ precipitates using the following sequence [48,49]:

SSS→GPB zone→S″/GPB2→S′ and S (Al_2CuMg)

While the exact nature of this sequence via the formation of GPB zones is still receiving considerable attention [48,49], the final product is the S phase having a needle or lath aspect and 12 possible variants. Several authors consider that the S′ to S transition is rather continuous; the two phases having similar crystallography but slightly different lattice parameters and, consequently, different degrees of coherency with the Al matrix [44].

Fig. 2 shows a low magnification EBSD map of the 2024 Al alloy sheet (Fig. 2a) and the corresponding pole figures (Fig. 2b) of the sample. The map confirms the general elongation of the grains along the rolling direction with grain length varying roughly from 10 to 500 μm. Within these grains, subgrains and low angle grain boundaries (LAGBs) are present as well as a certain degree of misorientation gradient resulting from the 15% room temperature plastic deformation. Fig. 2b shows the corresponding {001} and {111} pole figures giving the crystallographic texture of the material. The pole figures reveal crystallographic orientations that are very much consistent with the rolling texture of Al alloys [50,51]. The typical rolling texture in deformed Al alloys is known to be distributed along two tubes of orientations: the so-called "α-fibre" which runs from G orientation to the B orientation and the so-called "β-fibre" which contains the C orientation and meets the α-fibre at the B orientation [51].

Fig. 3 shows two backscattered SEM images of the top surface of the 2024 alloy after 15 pulses of HCPEB treatment. In comparison with Fig. 1a, the low magnification image in Fig. 3a reveals that the white contrasts corresponding to the large domains of constituent phases are fewer. The higher magnification image (Fig. 3b) shows some of these white domains having a blurred aspect (arrowed in black). The comparison of this higher magnification image with Fig. 1b and c is also interesting because it reveals the absence of any contrasts arising from (i) grain or sub-grain boundaries, (ii) T phase dispersoids and (iii) S phase precipitates. The global vanishing and blurred aspect of the domains of constituent phases can be explained by the repeated surface melting and rapid solidification of the alloy that induces liquid mixing and reduces the segregation scale [5,15] while the absence of precipitate and dispersoid is the result of the subsequent rapid cooling [23]. What is also visible at the surface after the HCPEB treatment in Fig. 3b is the presence of small black contrasts corresponding to small holes (arrowed in black). It is interesting to notice that these features are often visible in the vicinity of the white domains. Thus, these small holes do not correspond to the type of eruptive craters often observed in steels for example [3,10,13,26]. They are more probably the result of preferential evaporation of some species [4] of the constituant phases and/or shrinkage cavities forming during the solidification process.

Fig. 4 shows SEM images of the same 2024 alloy sheet after HCPEB but observed this time on cross-section. At the top surface (Fig. 4a), the thickness of the melted layer, 1 to 1.5 μm, can be clearly witnessed by the absence of the of the S and T phases and some blurred contrast of remaining chemical gradient arising from the dissolution of the constituting phases. Below this, in the middle and bottom parts of Fig. 4a, the presence of dispersoids of the T phase attests that the material was not melted. However, the slightly diffused aspect of these

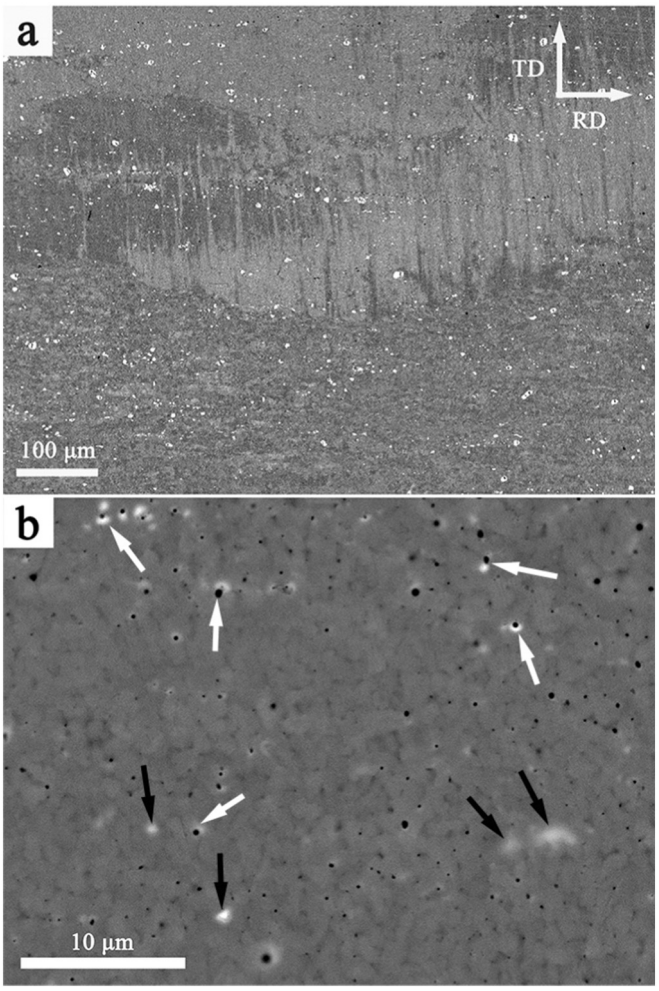

Fig. 3. BSE images of HCPEB treated sample in different magnification: 150× (a) and 3000× (b).The black arrows points to white domains while the white arrows points to the small holes located in the vicinity of the white domains.

dispersoids as well as the presence of faint contrasts of needle like precipitates suggest that the microstructure was affected by the heat transfer. It is also interesting to notice, as will be confirmed by EBSD in Fig. 6, that no grain boundary contrast was visible in Fig. 4a as well as along the first 5 μm below the top surface. Comparatively, Fig. 4b - that was taken 10 μm below the surface - does not witness any obvious microstructure modification: grains or sub-grains decorated by T dispersoids are visible (the S phase being impossible to resolve at this magnification).

EBSD analysis of the HCPEB modified surface, viewed from the top surface or from cross section, are given in Figs. 5 and 6, respectively. Fig. 5a is the orientation map of the treated surface while Fig. 5b is its corresponding band contrast quality map. Three different domains (labeled 1, 2 and 3 in Fig. 5a) can be clearly depicted in these images and their respective texture are represented by the corresponding {001} and {111} pole figures. Domains 1 and 2 are extremely large grains (several mm in length) having rather similar characteristics in terms of orientation: they corresponds to two specific orientations belonging to the B ("brass") component. Comparatively, domain 3 consists of several finer grains covering a much broader spectrum of orientations; actually rather similar to the texture of the initial material before HCPEB (Fig. 2b). The kikuchi quality map in Fig. 5b also gives interesting insights concerning some specificities of these domains. Apart from the grey or black dots rather aligned along RD, domains 1 and 2 display a rather bright contrast. This means that the Kikuchi patterns in these domains were of fairly good quality and suggests, as will be confirmed by

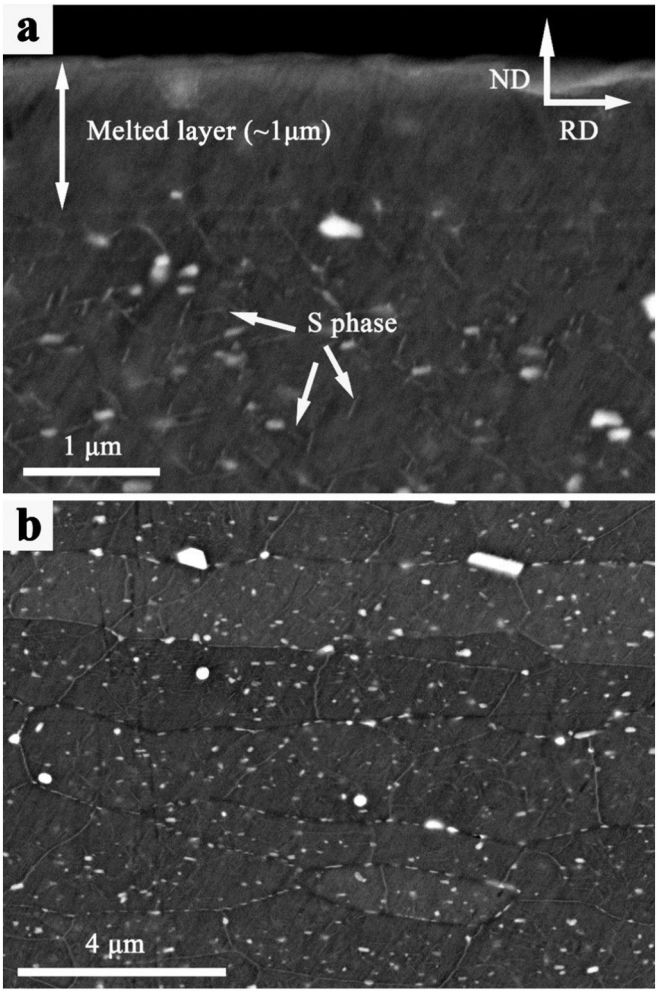

Fig. 4. Cross-sectional BSE images of the treated sample: (a) images of melted layer and (b) substrate taken from 10 mm below the surface.

the discussion of the mechanisms involved for their formation, that these two grains contained a low density of structural defects such as dislocations. Comparing the location of the black dots with the non-indexed zones in Fig. 5a and looking at the features displayed in Figs. 3a and 4a, it makes no doubt that the black dots correspond to non-indexed domains due to the presence of remaining constituent phases while the grey domains were difficult to index because the Al matrix was locally supersaturated in chemical species arising from the recent melting of these constituent phases. Looking at domain 3, the kikuchi map is of poorer quality, indicating that these areas contained a large quantity of structural defects.

The EBSD map carried out on cross section, Fig. 6a, reveals two types of domains in terms of crystallographic orientations. Almost all of the overall top surface is characterize by a single grain (having a blue color). Its orientation is consistent with the orientations of the grains labeled 1 and 2 in Fig. 5a: it has an orientation very close to the B component. It is also interesting to notice here that the thickness of these large grains reaches 6 to 8 μm, as seen at the surface in Fig. 6a. Thus, this grain does not only correspond to the melted layer seen in Fig. 4a: it is 3 to 4 times thicker than the melted layer. The rest of the map consists of grains or sub-grains represented with a broader range of colors (essentially greenish with bluish shades going towards pink and white - see the associated standard triangle) and non-indexed zones (in black). The black zones correspond to the secondary phases while, as confirmed by the pole figures in Fig. 6c, the broad range of colors illustrates the large distribution of orientations present in the α and β fibres characterizing the initial sheet before HCPEB (as depicted in Fig. 2b).

3.2. Effect of HCPEB on the single grain superalloys

Fig. 7 gathers information obtained at the surface of a single grain of AM1 superalloy of ⟨001⟩ orientation after 15 pulses of HCPEB irradiation. The EBSD analysis in Fig. 7b reveals that, despite having been melted 15 times, the top surface of the material retained its original ⟨001⟩ orientation. This means that the liquid has re-grown epitaxially from the subsurface solid. The cross section analysis given in Fig. 7c shows that the melted layer was about 3 μm thick. Consistently with previous works on HCPEB treated superalloys (including polycrystalline ones) [52,53], TEM revealed that the γ′ precipitates were completely dissolved in the melted pool which solidified as a supersaturated f.c.c. solid solution. The SEM image of the top surface (Fig. 7a) also shows two sets of parallel lines intersecting each other at 90°. These lines are very likely sliding traces of dislocations emerging at the surface. Indeed, superalloys deform by octahedral {111}⟨1−10⟩ slip and the traces of the octahedral planes form angles of 45° with the two cube axes of the [001] crystal [54]. They must have formed to relieve, by plastic deformation, the thermo-elastic stresses generated upon the fast cooling [55].

Fig. 8 shows another aspect of a single grain superalloy surface (here CMSX2) treated by HCPEB in the vicinity of an erupted crater. In most material for which electron beam irradiation has been applied, cratering is usually observed. These craters have been demonstrated to form by the combination of disparity in melting temperatures and heat extraction between the matrix and inclusions. Overheated, the sub-surface inclusions tend to vaporize and burst through the melted surface [3,10,13,26]. It has been established that craters form more easily at microstructure irregularities such as grain boundaries, phase boundaries and second phase particles [10,13,28,31,56,57]. In single grain superalloys, due to the absence of grain boundaries and coherency of the γ′ precipitates within their γ matrix, the crater density is extremely low [40]. In Fig. 8a, it is clear that the burst of the crater has modified the local stress and, consequently, modify the direction of the slip traces induced by the thermal stresses. In addition, the combination of Fig. 8b and c reveals that the nucleation of new grains has affected locally the efficiency of the epitaxial growth process.

4. Discussion

Clearly, the analysis of the 2024 alloy after HCPEB has revealed very interesting microstructure modifications that are rather unusual for HCPEB treated surfaces. In addition to the fact that a high number of publications have been dealing with the formation of “nanograins” after pulsed electron beam irradiation, one of the reasons why the observation of large grains that grew abnormally can be considered as a little surprising is due to the fact that it is hard to conceptualize the fact that such a solid state mechanism could be operative in a surface treatment process involving ultra-fast thermal cycle and rapid solidification (10^5 to 10^8 K/s) [15,23]. To understand completely the microstructure modifications encountered here, it is also important to take into account the possible occurrence of an epitaxial growth mechanism taking place during the rapid solidification process. The occurrence of these two mechanisms is recalled hereafter in the first section of the discussion (Section 4.1) while the possibility of formation of large grains under HCPEB is discussed in the second section together with potential technical limitations to generate these mechanisms (Section 4.2).

4.1. Evidence of abnormal grain growth and epitaxial growth

The presence of some extremely large grains at the surface of the 2024 Al treated samples can only be explained by the occurrence of an abnormal grain growth mechanism. Abnormal or discontinuous grain growth, also referred to as exaggerated or secondary recrystallization, is a grain growth phenomenon through which certain energetically favorable grains are growing at a high rate and at the expense of their neighbors. This results in a bimodal grain size distribution and,

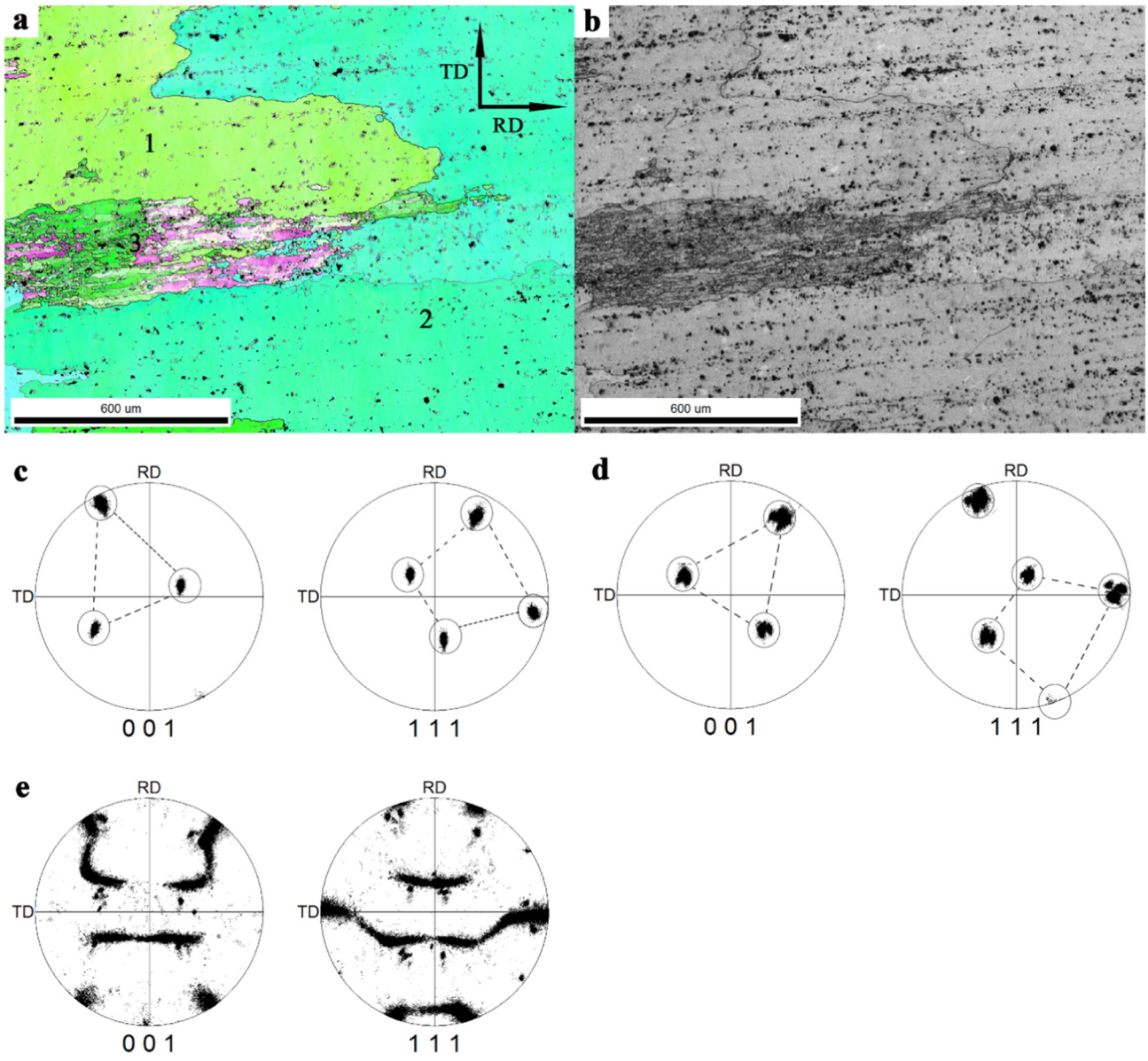

Fig. 5. EBSD maps and pole figure of the top surface of the HCPEB treated sample: orientation map of the treated surface (a), corresponding Kikuchi band contrast map (b), pole figures of large grain 1 (c), pole figures of large grain 2 (d) and pole figures of small grains located in domain 3 (e). Grey lines mean low angle grain boundaries ($\theta < 15°$) and black lines mean high angle grain boundaries ($\theta > 15°$) as presented in (a).black dots are non-indexed domains as presented in (a) and (b).

ultimately, in a microstructure dominated by a few very large grains. This is clearly what is depicted in Fig. 5. This mechanism is further confirmed by the orientation of the large grains that grew abnormally. Indeed, the secondary recrystallization does not proceed by nucleation of new grains but by the abnormal growth of grains that are already present in the initial microstructure [58]. Consistently with this mechanism, the large grains in Figs. 5 and 6 contain lower amounts of structural defects and their orientation, belonging to B ("brass") component, also belongs to the initial rolling texture characterized by the so-called "α + β" fibres. Comparatively, domains like the one labeled "3" in Fig. 5 still contain grains or subgrains with large misorientations (and a wide spread of orientation) as well as higher amount of structural defects. After melting, thanks to the epitaxial growth occurring during rapid solidification, this microstructure is frozen and the abnormal growth can occur again at the next pulsed irradiation.

For this process to occur repeatedly, it is important that the treated alloy authorizes epitaxial growth to take place. For this, it is of primary importance to avoid nucleation of new grains at the solid/liquid interface during re-solidification. This is clearly the case for the superalloys treated here. Indeed, for practical applications, this type of single grain superalloys can be repaired by epitaxial deposition using laser cladding, welding or brazing [59–61]. For example, even under the ultra fast rapid solidification occurring under laser cladding, epitaxial growth can take place if the primary phase in solidification remains the γ phase and even if the clad composition is different from the one of the substrate [59]. The same type of mechanism, where the grains of the substrate re-grow back-up through the melted layer towards the surface, has been observed in Al alloys treated by pulsed laser surface treatment [62]. Ryan and Prangnell [62] also demonstrated that this epitaxial growth was suppressed for Zr containing alloys in which the $L1_2$-Al_3Zr dispersoids were only partially melted and served as heterogeneous nucleation sites, resulting in a fine columnar grain structure. At this point of the discussion, it is important to recall that (i) the γ′ precipitates in our superalloys have a fully coherent interface with the γ matrix and that (ii) a domain of about 80 °C exists between their melting points and the onset of the of γ′ precipitation [63]. Since the primary phase in solidification is the γ matrix and not the precipitates, an epitaxial growth can take place leading to the reconstruction of the single grain.

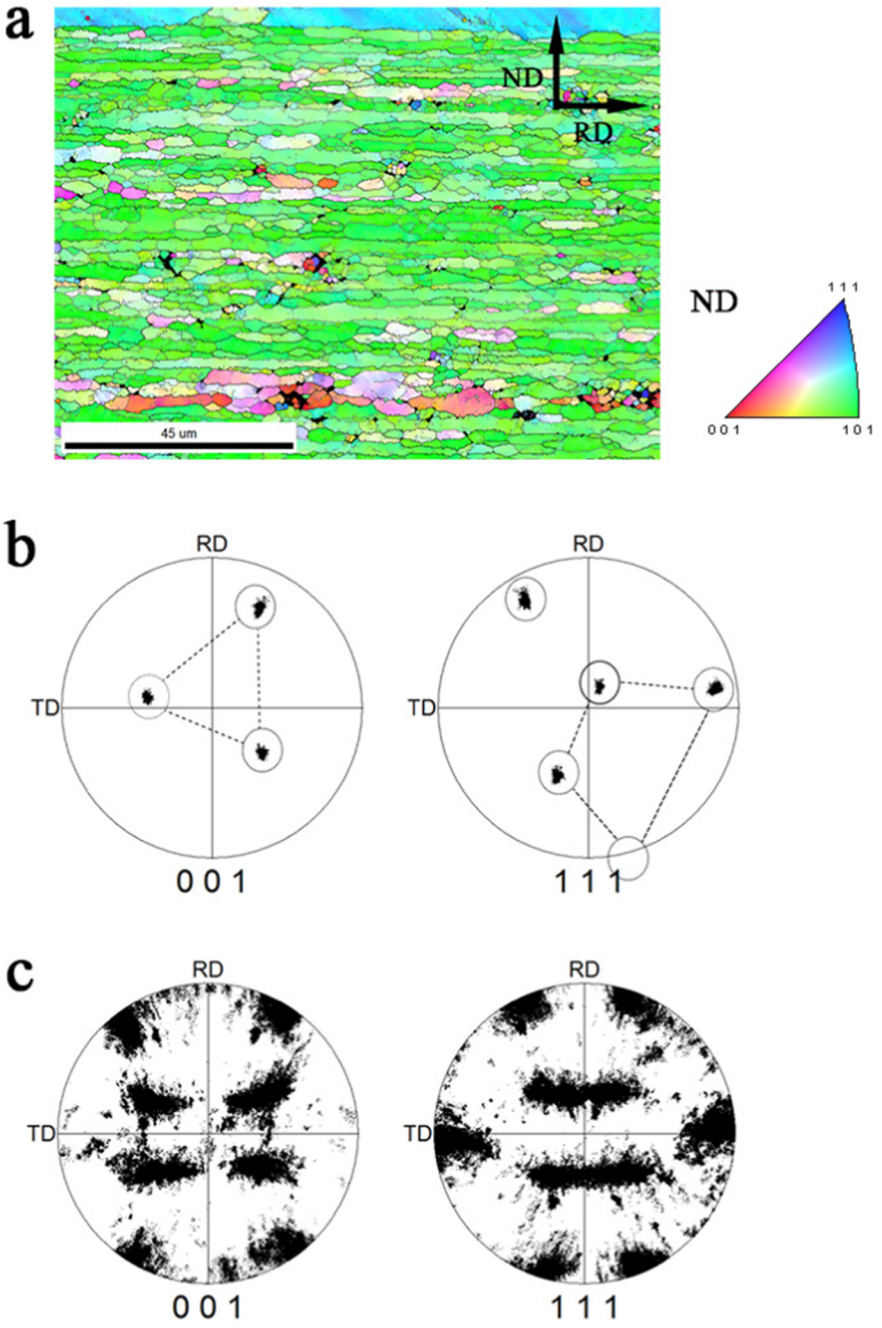

Fig. 6. EBSD maps and pole figures of treated sample on cross-sectional: orientation map (a), pole figure of large blue grain (b), and pole figure of the substrate grains (c). Grey lines mean low angle grain boundaries ($\theta < 15°$) and black lines mean high angle grain boundaries ($\theta > 15°$) as presented in (a).

We believe that this is also the reason why our results contrast with the interesting results obtained by Lv et al. [53] who observed fine twined grains after HCPEB irradiation of the polycrystalline GH4169 superalloy. In addition of the γ precipitates, this GH4169 alloy contained γ″ and δ precipitates that could serve as nucleation sites.

4.2. Formation of large grains under HCPEB and potential processing limitations

Abnormal or discontinuous grain growth is characterized by a subset of grains growing at a high rate and at the expense of their neighbors. In order for this to occur the subset of grains must possess some advantages over their competitors such as a high grain boundary energy, locally high grain boundary mobility, favorable texture or lower local second-phase particle density. The abnormal grain growth occurs here by the repeated complex cycles of rapid solidification/ultra-fast cooling/fast annealing processes which involve repeated straining and energy release within the microstructure. The ultra fast cooling generates an intense stress field that is accommodated by the formation of dislocations [55]. This is for example witnessed by the observation of slip traces on the surface of the superalloys in Figs. 7 and 8. On the subsequent HCPEB cycle, the fast heating authorizes the strain energy to be released by grain growth.

An important feature helping the development of abnormal grain growth is the presence of precipitates pinning the grain boundaries [58,64–67]. Indeed, the morphology of the grains is dictated by a bowing mechanism of the grain boundaries influenced by (i) the stored energy that provides the driving pressure for grain boundary migration and (ii) the non-uniformity of the particle distribution that modifies the local Zener drag and creates easier migration path for some grain

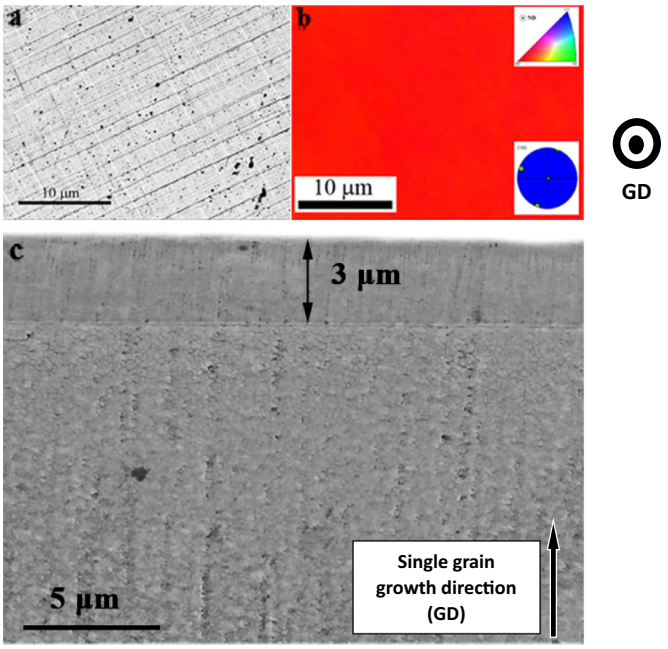

Fig. 7. Typical surface morphology on the treated AM1 (100) sample (a), its corresponding EBSD map with the inset of its (100) pole figure (b) and the SEM image of cross section morphology (c) of the 15-pulsed CMSX2 sample. GD indicates the growth direction of the single crystal cylindrical rod.

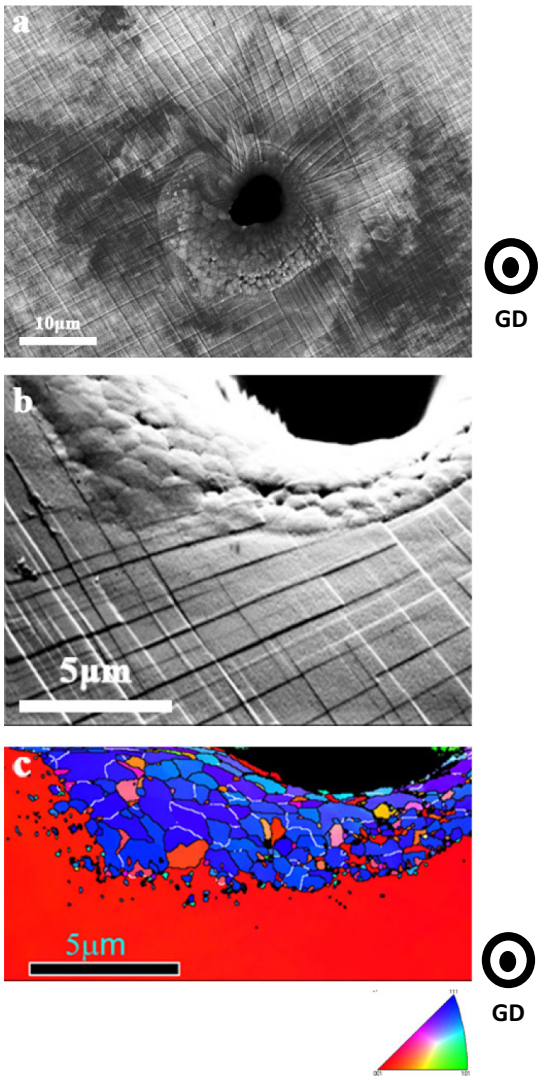

Fig. 8. SEM images of a crater (a), (b) and its corresponding EBSD map (c) on the surface of the 15-pulsed CMSX2 sample. GD indicates the growth direction of the single crystal cylindrical rod.

boundaries. An interesting observation about the large grains formed at the surface is that they could develop over a thickness (about 6 μm - Fig. 6a) far exceeding the melted zone (1.2 μm - Fig. 4a). This further support the combination of the two interacting mechanisms.

At each irradiation, the stored energy is renewed for all grains at the surface by the stress generated by the thermal gradient on cooling [55] which provides with new dislocations (as witnessed by the slip traces in Fig. 8 for the Ni superalloy for example). The exact nature of the structural defects so generated depends obviously on the orientation of the grains. Concerning the Al alloy, it is interesting to recall that the band contrast image in Fig. 5b revealed lower density of structural defects in the large grains that grew abnormally than in their surroundings. This gives, after each irradiation and despite the very short residence time (few μs) at high temperature, a regenerated driving force for successive strain-induced grain boundary migration for the abnormally growing surface grains having higher mobility in the RD-TD plane. Strain-induced boundary migration (SIBM) is a mechanism of grain growth that can occur at high temperature under small strains below the critical strain for dynamic recrystallization [68]. SIBM involves the bulging of a preexisting grain boundary, leaving a region behind the migrating boundary with a lower dislocation content, having the same orientation as the grain from which it has grown. Thus, the operation of this mechanism is expected to result in a recrystallization texture that is closely related to the initial (deformation) texture [58]. This is the case for the brass texture component in the case of our Al alloy. The driving force for SIBM is generally accepted to arise from a difference in dislocation content (stored energy) on each side of the grain boundary, the grain boundary moving towards the grain with the highest stored energy [58]. This is likely what is operating here repeatedly at each irradiation.

In addition, at each irradiation, the thermal gradient also generates a progressive dissolution of the precipitates in the heat-affected zone present below the melted domains. Thus, the progressive dissolution of the precipitates at the subsurface when the number of pulses increases generates, progressively, less pining on the migrating boundaries within the depth in the normal direction (ND). Thus, these surface grains become much thicker than the melted zone (and must not be mistaken with it). In short, the grain boundaries grow by a solid state mechanism on heating to release the energy that was stored on cooling. Then, just after their top surface melting, they have regrown epitaxially before getting strained again on subsequent solid state cooling.

In addition to the necessary requirements in terms of alloy composition authorizing (i) epitaxial solidification (absence of unmelted precipitates generating nucleation sites), (ii) abnormal grain growth (presence of precipitates inhibiting preferentially the growth of some grain boundaries) while (iii) avoiding the formation of too many eruptive craters that would nucleate new grains at their periphery, the control of some processing parameters is also required to grow grains abnormally under HCPEB. In particular, the energy of the pulsed beam and its duration are of particular importance. Under "low energy" conditions of pulsed beam irradiation, such as the ones provided by the "Nadezhda-2" equipment [1–3,15] or the "Hope-1" equipment [16,30] used here, the pulse durations are typically of the order of 1 to 5 μs for energy densities in the range 1 to 10 J/cm^2 which can generate a thickness of the melted layer usually in the range 1 to 10 μm. Comparatively, other facilities can develop more powerful beams that generate much thicker melted layers. For example, if the pulsed duration is increased to 100–200 μs and the energy density up to 30–80 J/cm^2 when using the "Solo" [69] machine, the melted layer thickness can reach several tens

of μm. When using a very high energy pulsed electron beam (50 and 150 J/cm^2 energy deposition) on a quenched and tempered steel, Markov and Rothstein, formed melted layers having a thicknesses of 25 μm and 180 μm [7]. Using the GESA accelerators developed at the Karlsruhe Institute of Technology (20–50 μs and 20–80 J/cm^2), melted layer thicknesses in the range 60–80 μm were reported for Al alloys [70] and 40 μm for steels [71]. For these very energetic beams, it is very likely that the thickness of the melted layer will not authorize the epitaxial growth - even if occurring initially - to be completed up to the top surface. For example, even with relatively low energy conditions, Samih et al. [40] found in a HCPEB treated AISI420 steel that the ferritic and austenitic phases solidified from the melt using two different mechanisms. The δ-ferrite formed first via an epitaxial growth mechanism onto the α-ferrite present in the sub-surface that was not melted. This growth from the substrate towards the top surface led to the formation of ferritic columnar grains, the diameter of which (2–3 μm) as well as their crystallographic orientations were inherited from the subsurface α precursors [40]. Comparatively, the austenite (γ) formed grains at the top surface using a nucleation controlled mechanisms using, presumably, remaining oxides present at the top surface of the melted layer [40]. Analysis of pulsed electron beam treated steels have also revealed gradients in the phases selected first from the melt [25] as well as in the morphology of the grains from columnar (sub-surface) towards equiaxed (at the top surface) [17] within the remelted layers.

Finally, while the epitaxial growth occurring during the rapid solidification process must generate the same texture as in the substrate when this mechanism occurs solely, the picture can be more complicated when a solid state phase transformation takes place subsequently on cooling. This is the case for example under irradiation of hexagonal metals such as Ti [23] or Zr [72] alloys for which a martenitic transformation takes place on cooling. In this case, and in contrast to the present results, significant textural changes were found that could be attributed to a strong selection of some martensitic variants due to the complex thermal and stress fields [72]. A detailed analysis of this variant selection has to be carried out to gain further insights and complement our understanding of the texture evolution encountered at the material surfaces after the HCPEB treatment.

5. Conclusion

One of the goals of this work was to demonstrate that pulsed electron beam treatments do not inevitably lead to significant grain refinement down to the sub-micrometer range. To demonstrate this, a commercial Al-Cu-Mg based alloy (2024 Al) and Ni-based single grain superalloys were treated by 15 pulses of HCPEB for an electron beam energy of 27 keV, an energy density of 6 J/cm^2 and a pulse duration of 1.5 μs.

Very large grains, millimetric in size, were obtained at the surface of the HCPEB treated Al2024 Al alloy. They have formed by the repeated combination of solid state phenomena and epitaxial re-solidification. These grains have boundaries that grow rapidly on heating to release the energy that was store on the previous rapid cooling. The repeated process is made possible because, just after their top surface melting, the microstructure re-grow epitaxially before getting strained again on subsequent solid state cooling.

Epitaxial growth was observed to take place in this work for the Al alloy and Ni-based superalloys. For this epitaxial growth to take place, it is of primary importance to (i) avoid nucleation of new grains at the solid/liquid interface during re-solidification and (ii) limit the formation of surface eruptive craters that would disrupt the growing process and generate the nucleation of new grains. The lateral size of these grains that grew epitaxially as well as their crystallographic orientation are directly inherited from their subsurface precursors.

Abnormal grain growth - secondary recrystallization - took place for the Al alloy where grains corresponding to the B ("brass") texture component developed to extremely large sizes (several mm in length). It is this difference in amount of structural defects that generates at each irradiation, and despite the very short residence time (few μs) at high temperature, the driving force for strain induced grain boundary migration. These structural defects are formed by the intense stress field generated on cooling that needs to be accommodated by plastic deformation and, in the case of our alloys, by the formation of dislocations. This plasticity was witnessed by the observation of slip traces on the surface of the single grain superalloys. As revealed for the Al alloy, the amount of stored energy and nature of structural defects depends on the orientation of the grains: a lower density of structural defects for in the grains that grew abnormally than in their neighbors.

Due to the renewed driving force at each pulse of irradiation, the grains that grow abnormally develop extensively along the RD-TD plane (along the surface) but also, because of the progressive dissolution of the precipitates that reduces the pining on the grain boundaries, within the depth in the normal direction (ND). A consequence of these mechanisms is that the thickness of these grains (6 to 8 μm) was about 4 to 5 times thicker than the thickness of the melted layer (up to 1.5 μm).

Authors contribution

Ping Yan has treated the Al samples and characterized the samples during his PhD work. Xiangdong Zhang has treated the superalloys and characterized the samples during his PhD work. Jianxin Zou has helped the students and supervised the PhD work of Ping Yan. Thierry Grosdidier has supervised the work of Xiangdong Zhang. Jianxin Zou and Thierry Grosdidier have conceptualized the research work. Thierry Grosdidier has written the manuscript, and given some help to analyse the data with the students. Jianxin Zou and Thierry Grosdidier have reviewed and verified the final version of the manuscript.

Acknowledgements

This work was supported by the French State through the program "Investment in the future" operated by the French National Research Agency (ANR) and referenced by ANR-11-LABX-0008-01 (Labex DAMAS). This work also was supported by the National Natural Science Foundation of China (No. 51271121, 51471109) and T.G. has benefited from a visiting position at SJTU through the "111" project of the China's Ministry of Education (B16032).

References

[1] D.I. Proskurovsky, V.P. Rotshtein, G.E. Ozur, et al., Pulsed electron-beam technology for surface modification of metallic materials, J. Vac. Sci. Technol. A 16 (1998) 2480–2488.
[2] D.I. Proskurovsky, V.P. Rotshtein, G.E. Ozur, et al., Physical foundations for surface treatment of materials with low energy, high current electron beams, Surf. Coat. Technol. 125 (2000) 49–56.
[3] G.E. Ozur, D.I. Proskurovsky, V.P. Rotshtein, A.B. Markov, Production and application of low-energy high current electron beams, Laser Part. Beams 21 (2003) 157–174.
[4] J.X. Zou, K.M. Zhang, T. Grosdidier, et al., Analysis of the evaporation and re-condensation processes induced by pulsed beam treatments, Int. J. Heat Mass Transf. 64 (2013) 1172–1182.
[5] J. Zou, T. Grosdidier, K. Zhang, C. Dong, Mechanisms of nanostructure and metastable phase formations in the surface melted layers of a HCPEB-treated D2 steel, Acta Mater. 54 (2006) 5409–5419.
[6] T. Grosdidier, J.X. Zou, N. Stein, et al., Texture modification, grain refinement and improved hardness/corrosion balance of a FeAl alloy by pulsed electron beam surface treatment in the "heating" mode, Scr. Mater. 58 (2008) 1058–1061.
[7] A.B. Markov, V.P. Rotshtein, Calculation and experimental determination of dimensions of hardening and tempering zones in quenched U7A steel irradiated with a pulsed electron beam, Nucl. Instrum. Methods B 132 (1997) 79–86.
[8] J.X. Zou, K.M. Zhang, S.Z. Hao, et al., Mechanisms of hardening, wear and corrosion improvement of 316 L stainless steel by low energy high current pulsed electron beam surface treatment, Thin Solid Films 519 (2010) 1404–1415.
[9] Y. Qin, J.X. Zou, C. Dong, et al., Temperature–stress fields and related phenomena induced by a high current pulsed electron beam, Nucl. Instrum. Methods B 225 (2004) 544–554.
[10] Y. Qin, C. Dong, Z. Song, et al., Deep modification of materials by thermal stress wave generated by irradiation of high-current pulsed electron beams, J. Vac. Sci. Technol. A 27 (2009) 430–435.

[11] K.M. Zhang, J.X. Zou, T. Grosdidier, et al., Surface modification of Ni (50.6 at.%) Ti by high current pulsed electron beam treatment, J. Alloys Compd. 434 (2007) 682–685.
[12] L.L. Meisner, M.G. Ostapenko, A.I. Lotkov, et al., Surface microstructure and B2 phase structural state induced in NiTi alloy by a high-current pulsed electron beam, Appl. Surf. Sci. 324 (2013) 44–52.
[13] K.M. Zhang, J.X. Zou, T. Grosdidier, C. Dong, Crater-formation-induced metastable structure in an AISI D2 steel treated with a pulsed electron beam, Vacuum 86 (2012) 1273–1277.
[14] D. Peng, Q. Guan, B. Chen, Deformation twinning in pure nickel induced by a high-current pulsed electron beam, Arab. J. Sci. Eng. 36 (2011) 1319–1325.
[15] V.P. Rotshtein, V.A. Shulov, Surface modification and alloying of aluminium and titanium alloys with low-energy, high-current electron beams, J. Metall. (2011), 673685. .
[16] S. Hao, S. Yao, J. Guan, A. Wu, P. Zhong, C. Dong, Surface treatment of aluminum alloy by high current pulsed electron beam, Curr. Appl. Phys. 1 (2001) 203–208.
[17] J.W. Murray, J.C. Walker, A.T. Clare, Nanostructures in austenitic steel after EDM and pulsed electron beam irradiation, Surf. Coat. Technol. 259 (2014) 465–472.
[18] Y. Uno, A. Okada, K. Uemura, et al., A new polishing method of metal mold with large-area electron beam irradiation, J. Mater. Process. Technol. 187–188 (2007) 77–80.
[19] J.C. Walker, J.W. Murray, M. Nie, et al., The effect of large-area pulsed electron beam melting on the corrosion and microstructure of a Ti6Al4V alloy, Appl. Surf. Sci. 311 (2014) 534–540.
[20] A. Okada, Y. Okamoto, Y. Uno, et al., Improvement of surface characteristics for long life of metal molds by large-area EB irradiation, J. Mater. Process. Technol. 214 (2014) 1740–1748.
[21] J. Kim, H.W. Park, Influence of a large pulsed electron beam (LPEB) on the corrosion resistance of Ti6Al7Nb alloys, Corros. Sci. 90 (2015) 153–160.
[22] J. Kim, W.J. Lee, H.W. Park, Temperature predictive model of the large pulsed electron beam (LPEB) irradiation on engineering alloys, Appl. Therm. Eng. 128 (2018) 151–158.
[23] X.D. Zhang, J.X. Zou, S. Weber, et al., Microstructure and property modifications in a near α Ti alloy induced by pulsed electron beam surface treatment, Surf. Coat. Technol. 206 (2011) 295–304.
[24] J.X. Zou, T. Grosdidier, B. Bolle, et al., Texture and microstructure at the surface of an AISI D2 steel treated by high current pulsed electron beam, Metall. Mater. Trans. A 38 (2007) 2061–2071.
[25] C.L. Zhang, Q. Gao, P. Lv, et al., Surface modification of Cu-W powder metallurgical alloy induced by high-current pulsed electron beam, Powder Technol. 325 (2018) 340–346.
[26] K. Zhang, J. Zou, T. Grosdidier, C. Dong, D. Yang, Improved pitting corrosion resistance of AISI 316L stainless steel treated by high current pulsed electron beam, Surf. Coat. Technol. 201 (2006) 1393–1400.
[27] H. Xia, C.L. Zhang, P. Lv, et al., Surface alloying of aluminum with molybdenum by high-current pulsed electron beam, Nucl. Inst. Methods B416 (2018) 9–15.
[28] C.L. Zhang, P. Lv, J. Cai, et al., Enhanced corrosion property of W-Al coatings fabricated on aluminum using surface alloying under high-current pulsed electron beam, J. Alloys Compd. 723 (2017) 258–265.
[29] H. Xia, H.Y. Liu, C.L. Zhang, et al., The microstructure and mechanical properties of Pb alloying layer on Al using surface alloying by high-current pulsed electron beam, Mat. Res. Express 4 (2017), 116523. .
[30] S.Z. Hao, L.M. Zhao, Y.L. Zhang, et al., Improving corrosion and wear resistance of FV520B steel by high current pulsed electron beam surface treatment, Nucl, Inst. Methods Phys. Res. B 356–357 (2015) 12–16.
[31] J. Cai, K.M. Zhang, Z.M. Zhang, et al., Surface nanostructure formations in an AISI 316L stainless steel induced by pulsed electron beam treatment, J. Nanomater. (2015), 796895. .
[32] C. Zhang, J. Cai, P. Lv, et al., Surface microstructure and properties of Cu-C powder metallurgical alloy induced by high current pulsed electron beam, J. Alloys Compd. 697 (2017) 96–103.
[33] G. Tang, D. Luo, G. Fan, X. Ma, L. Wang, Strengthening effect of nano-scaled precipitates in Ta alloying layer induced by high current pulsed electron beam, Nucl. Inst. Methods Phys. Res. B 398 (2017) 9–12.
[34] T. Grosdidier, J.X. Zou, B. Bolle, et al., Grain refinement, hardening and metastable phase formation by high current pulsed electron beam (HCPEB) treatment under heating and melting modes, J. Alloys Compd. 504 (2010) S508–S511.
[35] J.W. Dong, K.M. Zhang, Y. Cai, Z.M. Zhang, Y. Lei, T. Zhang, Formation of ultrafine-grained Ti3Al on a Ti48Al2Cr2Nb intermetallic alloy induced by pulsed electron beam treatment, J. Nanomater. (2015), 389594. .
[36] S. Hao, M. Li, Producing nano-grained and Al-enriched surface microstructure on AZ91 magnesium alloy by high current pulsed electron beam, Nucl. Instrum. Methods B 375 (2016) 1–4.
[37] M.C. Li, S.Z. Hao, H. Wen, et al., Surface composite nanostructures of AZ91 magnesium alloy induced by high current pulsed electron beam treatment, Appl. Surf. Sci. 303 (2014) 350–353.
[38] Z.Y. Han, J. Han, Z.Z. Jing, Surface microstructure of nanoaluminized CoCrAlY coating irradiated by HCPEB, J. Nanomater. (2016), 7124218. .
[39] H. Wang, S. Hao, Surface nanostructure and improved microhardness of 40CrNiMo7 steel induced by high current pulsed electron beam treatment, Nucl. Inst. Methods Phys. Res. B 403 (2017) 45–50.
[40] Y. Samih, G. Marcos, N. Stein, et al., Microstructure modifications and associated hardness and corrosion improvements in the AISI 420 martensitic stainless steel treated by high current pulsed electron beam (HCPEB), Surf. Coat. Technol. 259 (2014) 737–745.
[41] K. Harris, G.L. Erickson, R.E. Schwer, Proceedings of the "High Temperature Alloys for Gas Turbines and Other Applications" Liège - B, D. Reidel Publishing Company, 1986 709.
[42] P. Caron, T. Khan, Mater. Sci. Eng. A 61 (1983) 173.
[43] T. Grosdidier, A. Hazotte, A. Simon, On the dissolution of coherent precipitates in Ni-based single crystal superalloys, Scr. Met. Mater. 30 (1994) 1257–1262.
[44] S.C. Wang, M.J. Starink, Precipitates and intermetallic phases in precipitation hardening Al–Cu–Mg–(Li) based alloys, Int. Mater. Rev. 50 (2005) 193–215.
[45] R.G. Buchheit, R.P. Grant, P.F. Hlava, et al., Local dissolution phenomena associated with S phase (Al_2CuMg) particles in aluminum alloy 2024T3, J. Electrochem. Soc. 144 (1997) 2621–2628.
[46] B. Zhang, J. Wang, B. Wu, et al., Direct observation of atomic-scale origins of local dissolution in Al-Cu-Mg alloys, Sci. Rep. 6 (2016) 39525.
[47] Y.Q. Chen, S.P. Pan, W.H. Liu, et al., Morphologies, orientation relationships, and evolution of the T-phase in an Al-Cu-Mg-Mn alloy during homogenisation, J. Alloys Compd. 709 (2017) 213–226.
[48] S.C. Wang, M.J. Starink, N. Gao, Precipitation hardening in Al–Cu–Mg alloys revisited, Scr. Mater. 54 (2006) 287–291.
[49] S.C. Wang, M.J. Starink, Two types of S phase precipitates in Al–Cu–Mg alloys, Acta Mater. 55 (2007) 933–941.
[50] O. Engler, J. Hirsch, K. Lücke, Texture development in Al 1.8 wt% Cu depending on the precipitation state—I. Rolling textures, Acta Metall. 37 (1989) 2743–2753.
[51] J. Hirsch, K. Lücke, Mechanism of deformation and development of rolling texture in polycrystalline FCC metals: I, description of rolling texture development in homogeneous Cu Zn alloys, Acta Metall. 36 (1988) 2863–2882.
[52] S.Z. Hao, X.D. Zhang, X.X. Mei, et al., Surface treatment of DZ4 directionally solidified nickel-based superalloys by high current pulsed electron beam, Mater. Lett. 62 (2008) 414–417.
[53] P. Lv, X. Sun, J. Cai, et al., Microstructure and high temperature oxidation resistance of nickel based alloy GH4169 irradiated by high current pulsed electron beam, Surf. Coat. Technol. 309 (2017) 401–409.
[54] S.L. Semiatin, P.N. Fagin, M.G. Glavisic, D. Raabe, Deformation behavior of Waspaloy at hot-working temperatures, Scr. Mater. 50 (2004) 625–629.
[55] K.M. Zhang, J.X. Zou, B. Bolle, et al., Evolution of residual stress states in surface layers of an AISI D2 steel treated by low energy high current pulsed electron beam, Vacuum 87 (2013) 60–68.
[56] Z. Zhang, S. Yang, P. Lv, et al., The microstructure and corrosion properties of polycrystalline copper induced by high-current pulsed electron beam, Appl. Surf. Sci. 294 (2014) 9–14.
[57] L.J. Chai, Z.M. Zhou, Z.P. Xiao, et al., Evolution of surface microstructure of Cu-50Cr alloy treated by high current pulsed electron beam, Sci. China Technol. Sci. 58 (2015) 462–469.
[58] A. Rollett, G.S. Rohrer, J. Humphreys, in: Newnes (Ed.), Recrystallisation and Related Annealing Phenomena, third edition, 2017.
[59] C. Bezencon, A. Schnell, W. Kurz, Epitaxial deposition of MCrAlY coatings on a Ni-base superalloy by laser cladding, Scr. Mater. 49 (2003) 705–709.
[60] B. Laux, S. Piegert, J. Rosler, Fast epitaxial high temperature brazing of single crystalline nickel based superalloys, J. Eng. Gas Turbines Power 131 (2009), 032102. .
[61] R. Vilar, E.C. Santos, P.N. Ferreira, et al., Structure of NiCrAlY coatings deposited on single-crystal alloy turbine blade material by laser cladding, Acta Mater. 57 (2009) 5292–5302.
[62] P. Ryan, P.B. Prangnell, Grain structure and homogeneity of pulsed laser treated surfaces on Al-aerospace alloys and FSWs, Mater. Sci. Eng. A 479 (2008) 65–75.
[63] T. Grosdidier, A. Hazotte, A. Simon, Precipitation and dissolution processes in γ/γ′ single crystal nickel-based superalloys, Mater. Sci. Eng. A 256 (1998) 183–196.
[64] J. Harase, R. Shimizu, D.J. Dingley, Texture evolution in the presence of precipitates in Fe-3% Si alloy, Acta Metall. Mater. 39 (1991) 763–770.
[65] N. Rajmohan, J. Szpunar, Y. Hayakawa, A role of fraction of mobile grain boundaries in secondary recrystallization of Fe-Si steels, Acta Mater. 47 (1999) 2999–3008.
[66] S. Guessasma, E. Suzon, T. Grosdidier, F. Wagner, Static recrystallisation in an ODS FeAl alloy: the effect of particles on texture and anisotropic grain growth developments, Intermetallics 16 (2008) 1013–1025.
[67] C.S. Park, T.-W. Na, H.K. Park, et al., Misorientation characteristics of penetrating morphologies at the growth front of abnormally growing grains in aluminium alloys, Philos. Mag. Lett. 92 (2012) 344–351.
[68] Y. Yogo, H. Takeuchi, T. Ishikawa, et al., Strain-induced boundary migration of carbon steel at high temperatures, Scr. Mater. 61 (2009) 1001–1003.
[69] V.V. Uglov, A.K. Kuleshov, E.A. Soldatenko, et al., Structure, phase composition and mechanical properties of hard alloy treated by intense pulsed electron beams, Surf. Coat. Technol. 206 (2012) 2972–2976.
[70] R. Fetzer, G. Mueller, W. An, A. Weisenburger, Metal surface layers after pulsed beam treatment, Surf. Coat. Technol. 258 (2014) 549–556.
[71] W. An, Ya E. Krasik, R. Fetzer, et al., Characterization of high-current elevtron beam interaction with metal targets, J. Appl. Phys. 110 (2011), 093304. .
[72] L. Chai, B. Chen, S. Wang, et al., Microstructural, textural and hardness evolution of commercially pure Zr surface-treated by high current pulsed electron beam, Appl. Surf. Sci. 390 (2016) 430–434.